Nature Communications

https://doi.org/10.1038/s41467-026-71170-z

Article in Press

# Direct visualization of the existence of surface local chemical order in a high-entropy CoCrFeMnNi alloy

Received: 24 June 2025

Accepted: 13 March 2026

Cite this article as: Kim, L., Sharma, P., Tsai, C.-W. *et al.* Direct visualization of the existence of surface local chemical order in a high-entropy CoCrFeMnNi alloy. *Nat Commun* (2026). https://doi.org/10.1038/s41467-026-71170-z

**Lauren Kim, Prince Sharma, Che-Wei Tsai, E-Wen Huang, Peter K. Liaw, Jien-Wei Yeh, Ganesh Balasubramanian & TeYu Chien**

# Direct visualization of the existence of surface local chemical order in a high-entropy CoCrFeMnNi alloy

Lauren Kim[1†], Prince Sharma[2], Che-Wei Tsai[3,4], E-Wen Huang[4,5], Peter K. Liaw[6], Jien-Wei Yeh[3,4], Ganesh Balasubramanian[7], and TeYu Chien[1,8*]

[1]Department of Physics & Astronomy, University of Wyoming, Laramie, WY 82071, USA

[2]Hopkins Extreme Materials Institute, Johns Hopkins University, Baltimore, MD 21218, USA

[3]Department of Material Science and Engineering, National Tsing Hua University, Hsinchu 30013, Taiwan

[4]High Entropy Materials Center, National Tsing Hua University, Hsinchu 30013, Taiwan

[5]Department of Materials Science and Engineering, National Yang Ming Chiao Tung University, Hsinchu 30010, Taiwan

[6]Department of Materials Science and Engineering, University of Tennessee, Knoxville, TN 37996, USA

[7]Department of Mechanical & Industrial Engineering, University of New Haven, West Haven, CT 06516, USA

[8]Center for Quantum Information Science and Engineering, University of Wyoming, Laramie, WY 82071, USA



Corresponding author. Email: †lkim1@uwyo.edu; *tchien@uwyo.edu

**Abstract**

The impacts of local chemical order (LCO) on the physical properties of high-entropy alloys (HEAs), have been widely discussed. However, the difficulty in unambiguously observing LCO with high precision poses a great challenge in establishing microscopic mechanisms regarding the impacts of LCO on physical properties. Furthermore, it is still unclear whether the LCO extends to HEA surfaces, which may impact surface-based properties, such as corrosion, oxidation, and catalytic activities. Through the utilization of scanning tunneling microscopy (STM), two surface LCO domains with corresponding $\sqrt{5} \times \sqrt{5} R \pm 26.6°$ quasi-long-range orderings (QLRO) are directly observed on a CoCrFeMnNi surface. Density functional theory (DFT) calculations identify the LCO within QLRO supercells. The findings provide evidence of the existence of surface LCO and demonstrate a method to directly observe the surface LCO of HEAs. With the ability to unambiguously resolve elemental configuration at atomic scale, the understanding of how LCO influences surface-based properties can be achieved, facilitating the design of HEAs with tailored functionalities.

## Introduction

Since the first realization in 2004[1,2], high-entropy alloys (HEAs) have gained increasing attention due to a variety of promising properties and tunability in refractory applications[3], ductility[4], mechanical strength[4], creep resistance[5], and electrocatalytic performance[6]. In addition to having good combinations of multiple mechanical properties, HEAs host a multitude of design options, such as changing elements and molar ratios among the elements. An emerging way to further enhance and tune properties of HEAs is through the manipulation of local chemical order (LCO), including chemical short-range order (CSRO) which has been shown to impact structural stability [7], hardness[8], strength[9], stacking fault energy[10], corrosion[11], magnetization[12], and electrochemical behavior[13], as well as enhance resistance to fatigue[14] and irradiation damage[15]. Some of the physical properties, such as corrosion resistance, oxidation resistance, and catalytic activities, are presumably greatly impacted by the surface atoms. While the existence of the surface LCO is still elusive, it is crucial to determine if the surface LCO does exist and, if it does, what kind of surface LCO can be found. These types of information will facilitate the understanding of the impact of LCO on surface-based properties of HEAs.

In equimolar HEAs, the existence of CSRO has been extensively discussed[16–19]. While the formation of CSRO can be thermodynamic[20] or mechanistic[17], its impact on the structural properties of HEAs is still one of the main debates in the field[8,20–26]. Some reports show that CSRO has a strong impact on mechanical properties[27] while others do not find a similar conclusion[24]. A primary reason for these contentious results is because CSRO is very difficult to be explicitly measured through existing characterization techniques. Most of the reported CSRO relies on scattering-based techniques such as X-ray, neutron, and electron scattering[8,23,28–30]. CSRO is proposed to appear as extra features in the regions of the reciprocal space with smaller

wavenumbers compared to the lattice Bragg peaks[16,17]. However, the observed extra features in diffraction can have multiple origins[19,31], resulting in challenging identification of CSRO. On the other hand, energy dispersive X-ray spectroscopy (EDX) mapping using scanning transmission electron microscopy (STEM) can supposedly provide atomic resolution images with elemental sensitivity. However, since STEM measures columns of atoms that consist of all possible elements in HEAs, it can only provide the elemental compositions in each column of atoms[32], failing to offer detailed elemental distributions at the atomic scale. Atom probe tomography (APT) is another tool capable of revealing preferential neighboring elements with nm-scale resolution[22,33]. However, the viability of APT in deciphering the CSRO remains inconclusive[19,31,34].

In contrast, techniques using scanning tunneling microscopy (STM) are capable of revealing atomic-scale images and sometimes element-sensitive information on the surfaces of metals, making it potentially ideal for resolving CSRO in HEAs. STM is well-known for offering high spatial resolution down to the atomic scale[35,36]. However, STM probes the electronic local density of states (LDOS) near the Fermi energy, which typically does not contain elemental information. Recently, by combining synchrotron X-rays with STM (namely SX-STM), SX-STM was demonstrated to be capable of detecting core level electrons with superior spatial resolution in various material systems[37,38], including HEAs with sub-nm scale elemental distributions mappings[39]. However, to clearly reveal and establish statistics of the LCO on HEA surfaces, this requires a much larger SX-STM dataset on the elemental distributions than that reported previously (~1.5 × 2.5 $nm^2$)[39]. With limited synchrotron beamtime, it is very challenging to reveal LCO in HEAs using SX-STM. On the other hand, although STM is considered insensitive to elements, limited examples exhibiting element-sensitive STM images

have been reported[40–46] with the following possible mechanisms: (i) differences in the work function (Cu on Mo(110)[43]) ; (ii) differences in the tunneling matrix ($Pt_{25}Ni_{75}$(111)[44]); (iii) differences in the surface states (Fe alloying with Cr(100)[45]); and (iv) differences in DOS near the Fermi energy (Cu on W(110)[46], PdAg(100), and PdAg(111)[40]). Among these element-sensitive STM measurements, CSRO was discussed on (111) and (110) facets of $Pt_{25}Co_{75}$[41] and PtNi(110) random alloys[42]. With these successful examples, it is argued that STM may be capable of distinguishing elements with atomic resolution in HEAs based on the subtle differences in the partial LDOS contributed by different elements near the Fermi energy. Here, with the assistance of density functional theory (DFT), the contrast seen with STM can be explained by the difference in the partial LDOS among different elements. The existence of surface LCO on a HEA surface is revealed, and two types of LCOs with corresponding quasi-long-range orders (QLROs) are clearly observed on the surface of a CoCrFeMnNi HEA. The results shown here provide a foundation to understand the surface LCOs and their potential impacts on the surface-based material properties of HEAs.



**Results and discussion**

**Observations of the surface ordering of CoCrFeMnNi**

The surface of the HEA is first characterized by low-energy electron diffraction (LEED), as shown in Fig. 1(b). It is observed to be a predominantly single crystal square lattice matching the pristine FCC (001) square lattice, depicted as the solid square in Fig. 1(a). The region inside the bright Bragg diffraction spots (circled white) in the LEED pattern [Fig. 1(b)] exhibits fuzzy features, indicating potential features on the surface with a longer length scale beyond the FCC square lattice. LEED usually has a featureless and isotropic background near the center of the image. This fact was used by Nascimento et. al.[47] to subtract the background to reveal a small

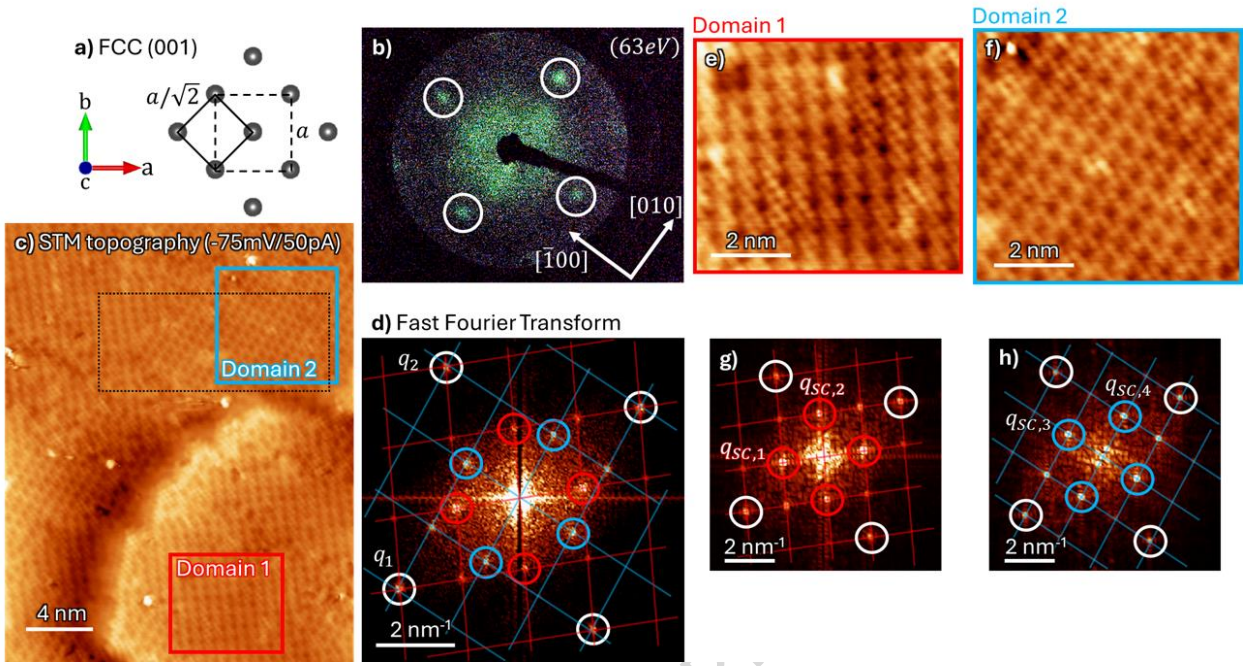


**Figure 1 | Low energy electron diffraction (LEED), scanning tunneling microscopy (STM) topography, and their fast Fourier transform images on CoCrFeMnNi surface. (a)** Structural model of the FCC (001) surface. The dashed square represents the pristine FCC unit cell, with labeled FCC lattice constant *a*, while the solid square represents the FCC (001) surface square lattice. **(b)** Low-energy electron diffraction (LEED) of the surface of the CoCrFeMnNi alloy. The diffraction spots due to the FCC (001) surface square lattice are highlighted with white circles. **(c)** STM topography measured at a set point of −75 mV; 50 pA. Two types of domains are revealed: domain 1 (red box) and domain 2 (blue box), where the cropped region (dotted black box) contains both domains. The corresponding **(d)** fast Fourier transform (FFT) image of the topography with red and blue circled peaks associated with the periodicity of domains 1 and 2, respectively. FCC (001) square lattice peaks are circled in white, and the FCC (001) surface square lattice periodicity is extracted by measuring the magnitudes of the reciprocal vectors $\boldsymbol{q}_1$ and $\boldsymbol{q}_2$. Enlarged topography images show clearer atomic resolution for **(e)** domain 1 and **(f)** domain 2 with **(g)** and **(h)** corresponding FFT images, respectively. The supercell periodicities in the two domains are measured by the magnitudes of the reciprocal vectors $\boldsymbol{q}_{SC,1}$, $\boldsymbol{q}_{SC,2}$, and $\boldsymbol{q}_{SC,3}$, $\boldsymbol{q}_{SC,4}$ for domain 1 and domain 2, respectively.

intensity of the diffraction spots buried inside the background signal. The fuzzy features near the center of LEED patterns were studied as diffuse LEED in literature towards the understanding of the surface disordered atoms[48,49]. However, the indistinct nature of the features prohibits clear understanding of this possible ordering. The electron beam spot size in LEED is in the order of hundreds of μm, indicating that the hazy LEED patterns are a direct result of the multi-grain measurements. Local measurements via STM can elucidate the origin of the ordering beyond the

FCC lattice ordering. Figure 1(c) shows a survey view of a STM topography in which two distinct domains are observed. The fast Fourier transform (FFT) of the topography image is shown in Fig. 1(d), where the white circled spots are FCC (001) square lattice peaks with an atom-atom spacing $d = 2.6 \pm 0.1$ Å, with additional peaks of the red and blue circled supercells towards the center of the plot. Unlike the LEED pattern, the FFT image of the STM topography presents sharp, bright features at wavenumbers smaller than the square lattice peaks, allowing for a detailed analysis of this extra order. As shown in Fig. 1(d), red and blue circled spots correspond to the two orderings in different domains where both domains show different orientations which are shown more clearly in the FFT images [Fig. 1(g) and 1(h)] of the cropped topography images [Fig. 1(e) and 1(f) respectively], where only one ordering that corresponds to one particular domain is present. The FCC(001) surface square lattice periodicity is extracted by measuring the magnitudes of the reciprocal vectors $\boldsymbol{q}_1$ and $\boldsymbol{q}_2$, which are defined as $|\boldsymbol{q}| = \frac{1}{d}$. In both domains, four supercell periodicities, $d_{\mathrm{SC}}$, are measured from the FFT images (Fig. 1(g) and (h), two $d_{SC}$ from each domain): $d_{\mathrm{SC},1} = 6.3 \pm 0.1$ Å, $d_{\mathrm{SC},2} = 5.8 \pm 0.1$ Å, $d_{\mathrm{SC},3} = 6.3 \pm 0.1$ Å, and $d_{\mathrm{SC},4} = 5.6 \pm 0.1$ Å, which are averaged to $\overline{d_{\mathrm{SC}}} = 6.0 \pm 0.1$ Å. The underlying FCC square lattice can be seen in the cropped topography [Figs. 1(e) and 1(f)]. It is clear that the square lattices in the two domains are identical, indicating that the two domains share the same underlying FCC square lattice. This is also confirmed in Fig. 1(d), where grid lines extend from red and blue domain peaks and meet at the FCC square lattice spots.

**$\sqrt{5} \times \sqrt{5}$ R $\pm$ 26.6° Quasi-long-range order (QLRO)**

The nature of the observed orderings in the two domains is revealed through a detailed analysis of the atomic-scale STM topography. Figure 2(a) shows an enlarged region of Fig. 1(c),

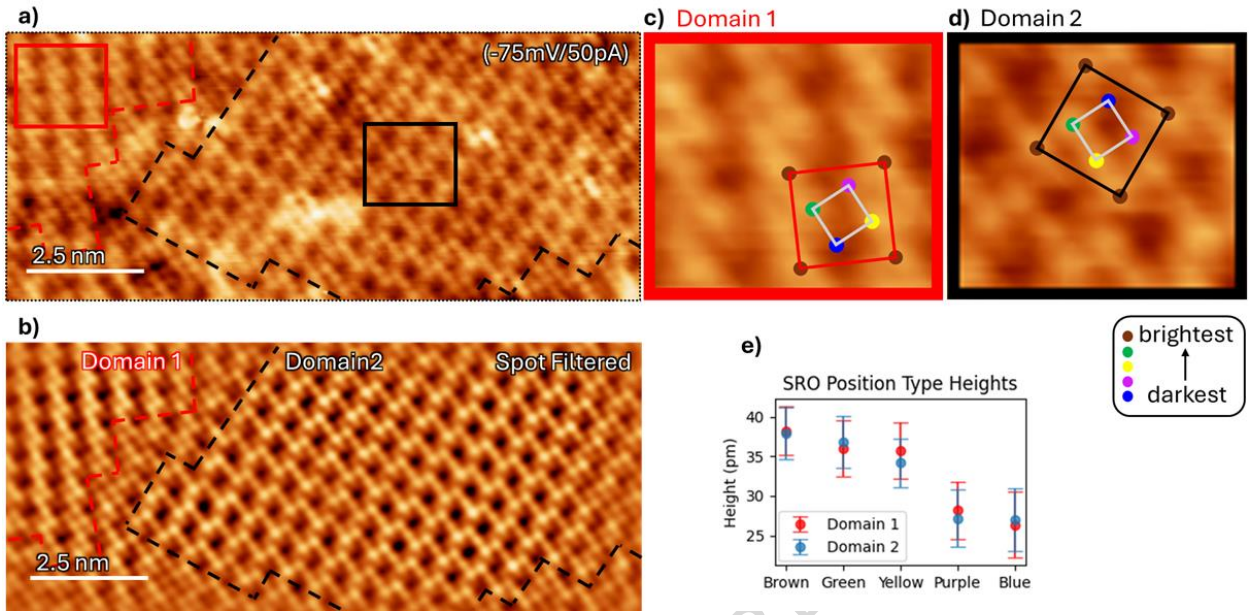


**Figure 2 | Definition of QLRO supercells and atomic sites and height analysis. (a)** STM topography enlarged view of Fig. 1(c) (dotted black box). **(b)** Spot-filtered image of the topography where domains 1 and 2 are marked. A domain boundary between domain 1 and 2 can be clearly seen. Supercells containing 5 unique position types labelled from brightest to darkest (brown, green, yellow, purple, and blue circles) are overlayed on **(c)** domain 1 (red square) and **(d)** domain 2 (black square) topography images. FCC square lattices are labeled with grey squares. **(e)** Measured distributions of atomic height depending on supercell position types. The error bar is defined by the full width half maximum (FWHM) of a Gaussian fitting function to the height histogram (see Supplementary Fig. 5-12).

exhibiting an area containing two neighboring domains with atomic resolution. A disordered region with a width of ~1 nm between the two ordered domains is observed. The domain boundary width varies slightly but remains in the order of ~1 nm. A domain boundary can be seen more clearly in the FFT spot-filtered topography in Fig. 2(b) (the spot-filtered process is described further in Supplementary Fig. 2). The two ordered domains exhibit a supercell periodicity corresponding to $\sqrt{5} \times \sqrt{5}$ R $\pm$ 26.6° with respect to the FCC (001) square lattice, as illustrated with red, blue and black squares in Figs. 2(c) and 2(d), respectively. The two patterns cannot be obtained by symmetrical operations from one to the other, meaning that they are not equivalent. It is worth noting that the elemental distribution of CoCrFeMnNi determined by SX-STM[39] exhibits a certain level of similarity to this ordering chemically, as depicted in

Supplementary Fig. 3. The apparent heights at each atomic location have been analyzed (see Supplementary Figs. 5-12) and summarized in Fig. 2(e). Here, the average height of the brightest atom (red atomic sites in Figs. 2(c) and 2(d) superlattices) in each STM image is used as a reference point as described in Supplementary Fig. 13. In Figs. 2(c) and 2(d), atomic sites are labeled with the ranking of the apparent heights (from highest to lowest: red, green, yellow, purple, blue) in both supercells. Upon closer inspection, the apparent heights of the atoms vary across different supercells, i.e. without explicit translational symmetry. Thus, the long-range order observed here is denoted as quasi-long-range order (QLRO). This is also the reason why the height uncertainty at each position type in Fig. 2(e) is about 3-5 pm. Considering the uncertainty in the apparent heights, two groups are defined: (i) three bright positions (red, green, and yellow) and (ii) two dark positions (purple and blue).

**Quantifying local distortion**

Furthermore, local distortions can be extracted and analyzed with the fitted atomic positions in STM images. The deviation of the displacement (same as the standard deviation of displacement) was used to quantify the local distortion in HEAs [50,51]. From the atomic resolution STM images, the atomic positions are determined using 2D center of mass (COM) fittings of the spot-filtered topography images (Supplementary Fig. 2). Two quantities are defined based on the fitted atomic positions to characterize the level of local distortion: (i) the standard deviation of the atom-atom distance $\sigma_{\mathrm{d}} = \sqrt{\sum_{i=1}^{N} \frac{1}{N} \left(d_i - \bar{d}\right)^2}$, where $\bar{d}$ is the average atom-atom distance, $d_i$ is the atom-atom distance of each pair of neighboring atoms, and $N$ is the total number of atom-atom pairs; and (ii) the average displacement $\bar{u}$ (see Table S1) and the standard deviation of the average displacement, $\sigma_u$. These two quantities are determined for domains 1, 2, and domain

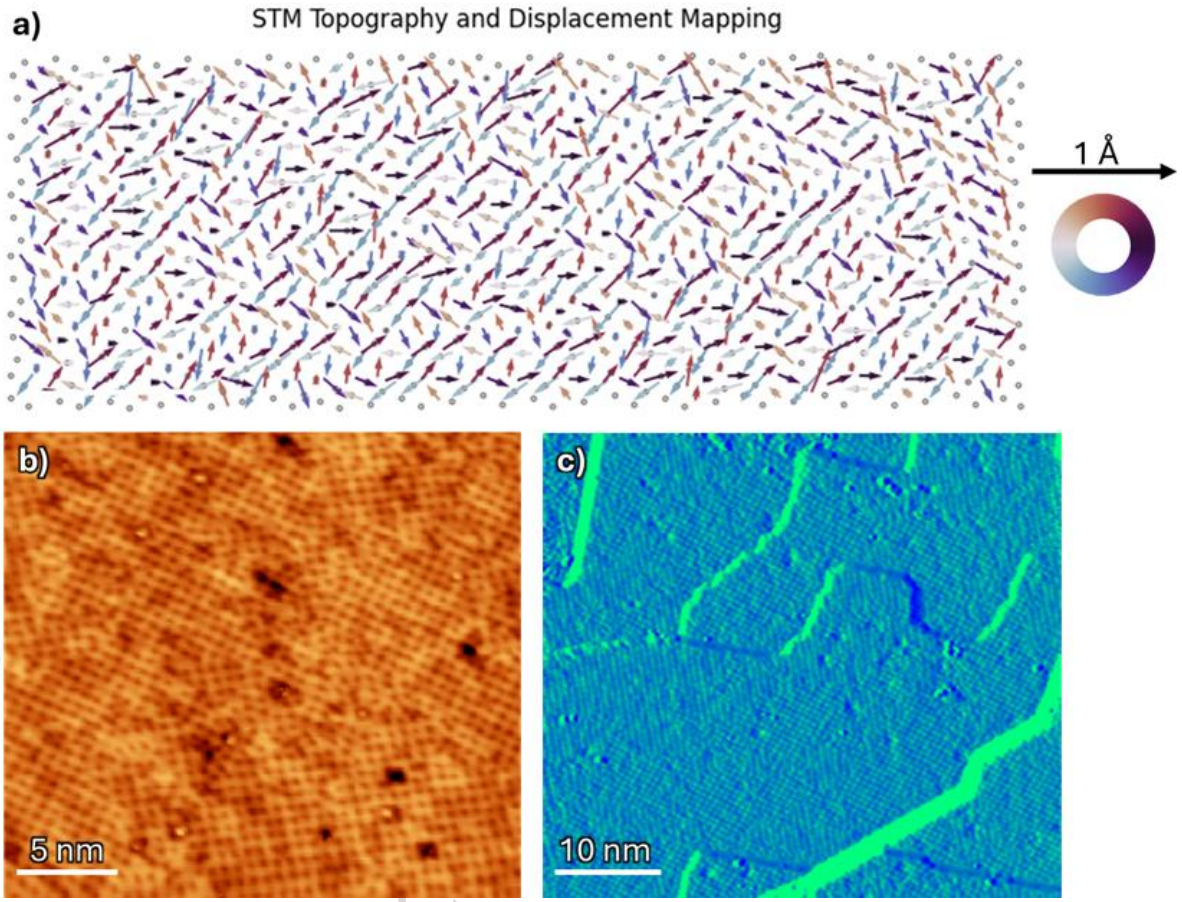


**Figure 3 | Lattice local distortion and QLRO domain distributions. (a)** Atom displacing mapping extracted from the STM topography (same as Fig. 2(a)). The vector lengths are plotted with a multiplicative factor of 40 for clear visualization. The color of the arrow is denoted based on the direction of the vector defined with the color wheel and the magnitude of the displacement is plotted with the scale bar next to the figure. **(b)** STM topographic image of a region where the domain sizes are in the order of a few nm; and **(c)** STM topography derivative image (d$z$/d$x$ mapping) of a region where the domain sizes are in the order of tens of $nm$. Setpoint for both STM images: 1 V; 300 pA.

boundaries (mixed regions) separately and are summarized in Table S1. Figure 3(a) shows a displacement mapping of the region presented in Fig. 2(a), with no clear ordering in the local distortion observed. The atom-atom distance in domain 1, 2, and domain boundary can be expressed as $\bar{d} \pm \sigma_d$: 2.69 ± 0.19 Å (domain 1), 2.67 ± 0.20 Å (domain 2), and 2.69± 0.19 Å (domain boundary). There is no clear difference in local distortion between the two domains and the domain boundary. The level of local distortion can be understood with the deviation of the atom-atom distance, which is determined to be ~7-8 % of the averaged atom-atom distance. The

local distortion in the five-element cantor alloy studied here exhibits a relatively high local distortion compared with refractory HEAs (~4 % to ~8 % in NbTaTiV and NbTaTiVZr)[50,51]. On the other hand, the statistics of the displacement $\bar{u} \pm \sigma_u$, is determined to be: $0.18 \pm 0.08$ Å (domain 1), $0.20 \pm 0.08$ Å (domain 2), and $0.17 \pm 0.08$ Å (domain boundary). Again, there is no clear difference in the average displacement between the two domains and the domain boundary. The average displacement is found to be the same as the standard deviation of the atom-atom distance, indicating that the deviation in the lattice constant (atom-atom distance) is the direct result of the local displacement at each atomic site. The two quantities essentially describe the same picture of local distortion in HEAs. These results indicate that the local distortion in HEA can be studied at different grains or regions (like dendritic vs interdenritic regions), which cannot be easily studied using scattering based techniques.

**QLRO domain distributions**

Three important questions remain: (i) are the two observed QLRO domains universal across different grains? (ii) are there preferred domain sizes or preferred domain types? And (iii) are there differences of the LCO in the dendritic or interdendritic region? For the first question, STM measurements shown in Fig. 2(a) and Supplementary Figs. 5-12 are taken within a vicinity of ~1 μm from each other. Figures 3(b) and 3(c) depict STM images taken at a location distanced ~sub-mm away. The same two types of QLRO (LCO) domains are observed in a different HEA crystalline grain (Supplementary Fig. 16). For the second question, the domain sizes may vary from a couple of nm to tens of nm as shown in Figs. 3(b) and 3(c). From the images observed, these two domains are often observed together (neighboring to each other), indicating energetically, no preferential domain between the two. This observation suggests that tuning LCO between the two types of domains is expected to be achievable with external stimuli, such

as thermal treatment or mechanical loadings. More research is needed to answer these questions. For the third question, due to the drastic difference in the length scale between the dendritic features (tens of micron) and the STM scanning size (tens of nm to hundreds of nm), it is challenging to determine the locations of the STM measurements belong to either dendritic or interdendritic regions.

**Origins of the QLRO**

There are a few possible origins to explain the observed QLRO. First, surface structural reconstructions occur on metal surfaces result in different surface ordering from the bulk structures, such as missing row (1×2) reconstruction on Pt(110)[52], (1×3) missing-row surface reconstruction on Be(11$\bar{2}$0) surface[53]. These types of surface reconstructions with missing atoms or with adatoms are ruled out. The height deviation among different sites is sub-angstrom, indicating that the contrast originates from a difference in electronic states rather than a physical atomic vacancy or adatom (Supplementary Fig. 17). Second, a charge density wave (CDW) is ruled out since there is no observable transition in *R*-*T* measurements reported for the Cantor alloy[54] and a Peierls transition is not experimentally observed in STM displacement mappings [Fig. 3(a)]. Third, the local chemical orders (LCO) may be the origin. As discussed, the contrast among different atomic sites in the supercell is electronic in nature. Based on the STM tunneling mechanism, it could be explained by the differences in either the tunneling matrix or the LDOS caused by different elements. Either way, the observed QLRO is associated with LCO. For the CoCrFeMnNi alloy, the elements have similar electron configurations near the Fermi energy. Thus, the tunneling matrices between different elements and the tungsten tip are expected to be similar. It is most likely that the origin of contrast is due to the subtle differences in LDOS belonging to different elements near the Fermi energy. One may also consider this as a type of

surface structural reconstruction based on the elemental ordering. This depends on whether the surface LCO is simply extended from the existing bulk LCO, or if the surface has its own unique LCO due to the existence of the surface. Without detailed information about the bulk LCO, it is inconclusive either way, and further research comparing the surface and bulk LCOs is required to address this question. Finally, the observed QLRO may simply be due to local corrugation (lattice distortion in the direction normal to the surface). While it is possible that the sub-angstrom corrugation of atomic height exists, the ordered surface corrugation is likely also associated with ordered elemental distributions, and this mechanism still ties to the existence of the surface LCO.

To further identify the origin of the observed contrast in topography, DFT calculations are performed to assist in assigning elements to atomic sites in the two QLRO domains. DFT calculations are performed on a slab of the alloy with randomly distributed elements, as shown in Fig. 4(a). In the STM constant current mode measured on a particular atomic plane, the STM apparent height is mainly determined by three factors: (i) atomic corrugation, (ii) tunneling matrix, and (iii) LDOS. First, due to different element sizes, HEA surfaces with different elements are expected to exhibit surface corrugation on a sub-atomic scale. The DFT calculation of the slab [Fig. 4(a)] with surface atoms relaxed can simulate the atomic corrugation. As shown in Supplementary Fig. 18, the surface corrugation is ~2 pm, which is smaller than the observed height differences (~10 pm) in the STM images, as exhibited in Fig. 2(e). It is clear that the surface corrugation is not enough to explain the observed height differences among the atomic sites in QLRO domains. Second, typically the tunneling matrix depends on the nature of the orbitals involved in the tunneling process. The elements in the HEA studied here are Co, Cr, Fe, Mn, and Ni, which are neighboring transition metals in the periodic table, all with $d$ orbitals. It is

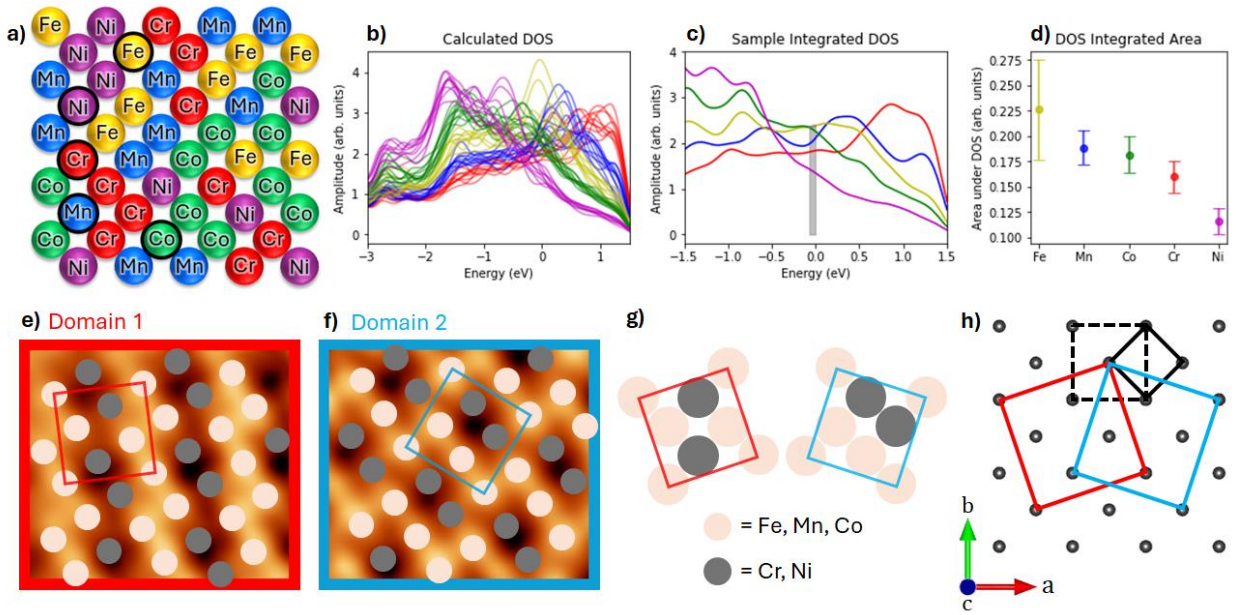


**Figure 4 | Elemental assignment with assistance of DFT calculated partial density of states.** **(a)** Model of the surface atoms of a randomly distributed equimolar slab with periodic boundary conditions that is used for DFT calculations. **(b)** DFT calculated partial LDOS for the surface atoms. The element type of the LDOS is denoted by the color of the curve in accordance with (a). **(c)** Cropped spectra near the Fermi energy for selected atoms (circled black) in (a). The shaded area indicates the integrated area between $-75$ and $0\ meV$. **(d)** The average and standard deviation distributions (error bars) of the integrated area under the curve (AUC) for all surface atoms in (a). **(e)** Domain 1 and **(f)** domain 2 spot-filtered STM topography with overlaid superlattices colored into two types of atoms (bright and dark). **(g)** Superlattice unit cells for each domain with bright and dark type atoms assigned using the calculated AUC rankings for the bright (Co, Fe, Mn) and dark (Cr, Ni) atoms. **(h)** Model of the FCC (001) surface with the surface unit cell (black solid), bulk FCC unit cell (black dashed), domain 1 supercell (red), and domain 2 supercell (blue).

expected that their tunneling matrices are very similar and thus ignored here. Therefore, the STM apparent heights $z_{\mathrm{STM}}$, can be related to the integration of the available LDOS as $z_{\mathrm{STM}} \propto \int_{-V_{\mathrm{b}}}^{0} \rho_{\mathrm{s}}(\epsilon) d\epsilon$, where $V_{\mathrm{b}}$ is the STM scanning bias, and $\rho_{\mathrm{s}}(\epsilon)$ is the LDOS of the atom underneath the STM tip as a function of energy $\epsilon$ with respect to the Fermi energy. The partial LDOS near the Fermi energy from each element is calculated from DFT on the slab with randomly distributed elements [Fig. 4(a)] and is illustrated in Fig. 4(b). It is obvious that the partial LDOS shows clear differences between elements, while deviations can be found in each element group. This trend indicates that the partial LDOS has an elemental identity, while the

neighboring elements may influence the details of the partial LDOS. By integrating each partial LDOS from $-75$ meV to 0 meV (STM bias used in Figs. 1 and 2: $-75$ mV) which is depicted as the shaded area in Fig. 4(c), the relative STM apparent height differences can be estimated. The resulting areas under the curves (AUCs) are summarized in Fig. 4(d), revealing a ranking of brightest (largest integrated AUC) to darkest (smallest integrated AUC): Fe, Mn, Co, Cr, then Ni. Hence, the elemental assignments with the DFT calculated AUC are: Fe, Mn, and Co for the bright group; and Cr and Ni for the dark group. Note that the Fe exhibits biggest uncertainty in the AUC (Fig. 4(d)). This is due to the spectrum variation of Fe near Fermi energy is largest among the five elements near Fermi energy, where the STM experiment tip-sample bias was set (see Fig. 4(b)). Other elements also exhibit similar spectrum variation but away from the Fermi energy. Thus, the AUC calculated near Fermi energy exhibit largest uncertainty for Fe. Thus, the LCO in the two QLRO domains can be visualized in Figs. 4(e) and 4(f) for domains 1 and 2, respectively. Figure 4(g) summarizes the elemental assignment within the supercells of the two types of domains, while the supercells are illustrated in Fig. 4(h). The measured surface LCO does not match the reported $L1_1$ or $L1_2$ orderings of the CoCrFeMnNi[55], indicating that the surface LCO may not be necessarily an extension of the bulk LCO.

In summary, the existence of the surface LCO on CoCrFeMnNi surfaces is directly observed with atomic resolution STM images. Two QLRO domains with supercell periodicities corresponding to $\sqrt{5} \times \sqrt{5}\ \mathrm{R} \pm 26.6°$ orientations with respect to the pristine FCC (001) square lattice and domain boundaries with randomized elemental distributions are revealed. Detailed height analysis exhibited a bimodal distribution of superlattice position types, indicating a non-negligible level of elemental randomness across the QLRO domains. With assistance from DFT calculations, elemental assignments inside the QLRO domain supercells are made, as

summarized in Fig. 4(g). This work unambiguously provides direct evidence of the existence of the surface LCO with the detailed elemental arrangements on HEA surfaces. In addition, the results clearly demonstrated that STM is a valuable tool to study HEA systems with unprecedented information that cannot be obtained by other characterization tools. It is expected that this work will inspire further and more extensive studies on HEA surfaces, where future theoretical modelling may help elucidate the origins and mechanism of surface LCO, encouraging the HEA research community to include STM as a more commonplace characterization tool in the understanding of the HEA systems.

## Methods

### HEA materials synthesis

A nearly equimolar CrMnFeCoNi alloy was synthesized using arc melting under 1 atm of inert Ar gas, using equimolar ratios of high purity powders (>99.95%) of each constituent element. To ensure compositional homogeneity, each sample was over- turned and re-melted five times at ≈3500 K. The sample stayed on a water-cooled copper plate during melting and solidification to cool it to room temperature. The HEA was cut into a 1 mm thick slice, where one side was polished with 1200 grit sandpaper and 0.5 to 0.05 μm DIAMAT polycrystalline diamond paste, in preparation for STM measurements.

### XRD Characterization

Rigaku SmartLab X-Ray Diffractometer was used to carry out the X-ray diffraction measurements. The XRD measurements were conducted at room temperature using Cu K$\alpha$ radiation ($\lambda = 1.54$ Å), and 0.3 degree step size. XRD measurements determined that the bulk crystal structure is predominantly face-centered cubic (FCC) with lattice parameter $a = 3.59 \pm$

0.01 Å [Supplementary Fig. 1(b)], which infers a nearest neighbor atom-atom distance of $d = \frac{a}{\sqrt{2}} = 2.54$ Å [Fig. 1(a)].

**SEM and EDX**

Scanning electron microscope energy dispersive X-ray spectroscopy (SEM-EDX) measurements were carried out using a FEI Quanta 250 SEM equipped with tungsten electron source, equipped with Everhart-Thornley Detector backscattered electron detector, and Oxford Inca energy dispersive x-ray spectroscopy system (EDX). The electron acceleration energy was set to 20 kV. SEM-EDX measurements were used to determine the bulk chemical composition of the alloy to be $Co_{18}Cr_{20}Fe_{16}Mn_{26}Ni_{20}$, with EDX mappings shown in Supplementary Figs. 1(d)-(h) that display the typical dendritic structure for Cantor alloys fabricated via arc melting[56].

**STM measurements**

In preparation for STM measurements, the CoCrFeMnNi alloy was cleaned in ultra-high vacuum (UHV) via multiple cycles of warm $Ar^+$ ion sputtering (460 °C, 30 minutes) and annealing (510 °C, 30 minutes). The last cycle before STM measurements ended with a 24-hour annealing at 510 °C and a slow cooling process from 510 °C to 310 °C at a cooling rate of ~1 °C/5 minute. The sample was transferred to STM chamber without exposing to air right after the cleaning procedure. All the STM measurements were conducted using Omicron Low-Temperature STM (LT-STM) system at liquid nitrogen temperature (77 K). The topographic images were measured using constant current mode with the set points indicated in the figure captions.

**DFT Calculations**

All DFT calculations were performed using Vienna ab initio simulation package (VASP 5.4.4) using the projected augmented wave (PAW) [57,58]. A 200-atom CoCrFeMnNi-(001) supercell with 4 layers was constructed with a vacuum spacing of 15 Å. The atomic configuration was generated using the special quasi-random structure approach to approximate the random chemical disorder of the HEA [59]. The exchange-correlation interactions were described using the Perdew–Burke–Ernzerhof (PBE) functional within the generalized gradient approximation (GGA) [60]. A high plane-wave energy cutoff of 520 eV is applied, while Brillouin zone integrations are carried out using a Γ-centered k-point mesh with a smearing width of 0.01 eV [61]. The force and energy convergence criteria for DFT self-consistent calculations were set to $10^{-3}$ eV/Å and $10^{-6}$ eV, respectively. STM images were generated using the Tersoff-Hamann approach [62,63], which models the STM tip as an s-wave. In this approximation, the tunneling current I at tip position r and applied voltage V is proportional to the integrated local density of states (LDOS). The LDOS was calculated by integrating states within an energy window of ±0.5 eV around the Fermi level to capture the relevant tunneling states at typical experimental bias voltages.

**Data Availability**

Data is available upon request. The LEED, STM, and DFT calculated PDOS datasets generated during and analyzed during the current study are available in the figshare repository[64].



**References**


1. Yeh, J. W. *et al.* Nanostructured high-entropy alloys with multiple principal elements: Novel alloy design concepts and outcomes. *Adv. Eng. Mater.* **6**, 299–303 (2004).
2. Cantor, B., Chang, I. T. H., Knight, P. & Vincent, A. J. B. Microstructural development in equiatomic multicomponent alloys. *Materials Science and Engineering A* **375–377**, 213–218 (2004).
3. Dewangan, S. K. *et al.* A review on High-Temperature Applicability: A milestone for high entropy alloys. *Engineering Science and Technology, an International Journal* **35**, 101211 (2022).
4. Ma, E. & Wu, X. Tailoring heterogeneities in high-entropy alloys to promote strength–ductility synergy. *Nat. Commun.* **10**, 5623 (2019).

5. Wang, D., Tan, J., Li, C. J., Qin, X. M. & Guo, S. F. Enhanced creep resistance of Ti30Al25Zr25Nb20 high-entropy alloy at room temperature. *J. Alloys Compd.* **885**, 161038 (2021).

6. Kumar Katiyar, N., Biswas, K., Yeh, J.-W., Sharma, S. & Sekhar Tiwary, C. A perspective on the catalysis using the high entropy alloys. *Nano Energy* **88**, 106261 (2021).

7. Wang, D., Tan, J., Li, C. J., Qin, X. M. & Guo, S. F. Enhanced creep resistance of Ti30Al25Zr25Nb20 high-entropy alloy at room temperature. *J. Alloys Compd.* **885**, (2021).

8. Zhang, R. *et al.* Short-range order and its impact on the CrCoNi medium-entropy alloy. *Nature* **581**, 283–287 (2020).

9. Chen, S. *et al.* Simultaneously enhancing the ultimate strength and ductility of high-entropy alloys via short-range ordering. *Nat. Commun.* **12**, 4953 (2021).

10. Ding, J., Yu, Q., Asta, M. & Ritchie, R. O. Tunable stacking fault energies by tailoring local chemical order in CrCoNi medium-entropy alloys. *Proceedings of the National Academy of Sciences* **115**, 8919–8924 (2018).

11. Xie, Y. *et al.* A percolation theory for designing corrosion-resistant alloys. *Nat. Mater.* **20**, 789–793 (2021).

12. Walsh, F., Asta, M. & Ritchie, R. O. Magnetically driven short-range order can explain anomalous measurements in CrCoNi. *Proc. Natl. Acad. Sci. U. S. A.* **118**, e2020540118 (2021).

13. Lee, J. *et al.* Unlocking the potential of cation-disordered oxides for rechargeable lithium batteries. *Science (1979).* **343**, 519–522 (2014).

14. Zhang, Y. J., Han, D. & Li, X. W. Improving the stress-controlled fatigue life of low solid-solution hardening Ni-Cr alloys by enhancing short range ordering degree. *Int. J. Fatigue* **149**, 106266 (2021).

15. Lu, C. *et al.* Radiation-induced segregation on defect clusters in single-phase concentrated solid-solution alloys. *Acta Mater.* **127**, 98–107 (2017).

16. Han, Y. *et al.* Ubiquitous short-range order in multi-principal element alloys. *Nat. Commun.* **15**, 6486 (2024).

17. Yang, Y. *et al.* Rejuvenation as the origin of planar defects in the CrCoNi medium entropy alloy. *Nat. Commun.* **15**, 1402 (2024).

18. Beeson, W. B. *et al.* Single-Phase L10 -Ordered High Entropy Thin Films with High Magnetic Anisotropy. *Advanced Science* **11**, 2308574 (2024).

19. Walsh, F., Zhang, M., Ritchie, R. O., Minor, A. M. & Asta, M. Extra electron reflections in concentrated alloys do not necessitate short-range order. *Nat. Mater.* **22**, 926–929 (2023).

20. Sun, L. *et al.* Local chemical order enables an ultrastrong and ductile high-entropy alloy in a cryogenic environment. *Sci. Adv* **10**, eadq6398 (2024).

21. Chen, S. *et al.* Simultaneously enhancing the ultimate strength and ductility of high-entropy alloys via short-range ordering. *Nat. Commun.* **12**, 1–11 (2021).

22. He, M., Davids, W. J., Breen, A. J. & Ringer, S. P. Quantifying short-range order using atom probe tomography. *Nat. Mater.* **23**, 1200–1207 (2024).

23. Chen, X. *et al.* Direct observation of chemical short-range order in a medium-entropy alloy. *Nature* **592**, 712–716 (2021).

24. Li, L. *et al.* Evolution of short-range order and its effects on the plastic deformation behavior of single crystals of the equiatomic Cr-Co-Ni medium-entropy alloy. *Acta Mater.* **243**, 118537 (2023).

25. Yin, B., Yoshida, S., Tsuji, N. & Curtin, W. A. Yield strength and misfit volumes of NiCoCr and implications for short-range-order. *Nat. Commun.* **11**, 2507 (2020).

26. Zhang, R. *et al.* Direct imaging of short-range order and its impact on deformation in Ti-6Al. *Sci. Adv* **5**, eaax2799 (2019).

27. Sun, Z., Shi, C., Liu, C., Shi, H. & Zhou, J. The effect of short-range order on mechanical properties of high entropy alloy Al0.3CoCrFeNi. *Mater. Des.* **223**, 111214 (2022).

28. Yang, Y. *et al.* Determining the three-dimensional atomic structure of an amorphous solid. *Nature* **592**, 60–64 (2021).

29. Moniri, S. *et al.* Three-dimensional atomic structure and local chemical order of medium- and high-entropy nanoalloys. *Nature* **624**, 564–569 (2023).

30. Hsiao, H. W. *et al.* Data-driven electron-diffraction approach reveals local short-range ordering in CrCoNi with ordering effects. *Nat. Commun.* **13**, 6651 (2022).

31. Coury, F. G., Miller, C., Field, R. & Kaufman, M. On the origin of diffuse intensities in fcc electron diffraction patterns. *Nature* **622**, 742–747 (2023).

32. Zhu, G. *et al.* Constructing Structurally Ordered High-Entropy Alloy Nanoparticles on Nitrogen-Rich Mesoporous Carbon Nanosheets for High-Performance Oxygen Reduction. *Advanced Materials* **34**, 2110128 (2022).

33. Li, Y. *et al.* Quantitative three-dimensional imaging of chemical short-range order via machine learning enhanced atom probe tomography. *Nat. Commun.* **14**, 7410 (2023).

34. Walsh, F., Zhang, M., Ritchie, R. O., Asta, M. & Minor, A. M. Multiple origins of extra electron diffractions in fcc metals. *Sci. Adv* **10**, eadn9673 (2024).

35. Hamers, R. J. Atomic-Resolution Surface Spectroscopy with the Scanning Tunneling Microscope. *Annu. Rev. Phys. Chern.* **40**, 531–559 (1989).

36. Chen, C. J. Origin of Atomic Resolution on Metal Surfaces in Scanning Tunneling Microscopy. *Phys. Rev. Lett.* **65**, 448–451 (1990).

37. Shirato, N. *et al.* Elemental fingerprinting of materials with sensitivity at the atomic limit. *Nano Lett.* **14**, 6499–6504 (2014).

38. Ajayi, T. M. *et al.* Characterization of just one atom using synchrotron X-rays. *Nature* **618**, 69–73 (2023).

39. Kim, L. *et al.* Distinguishing Elements at the Sub-Nanometer Scale on the Surface of a High Entropy Alloy. *Advanced Materials* **36**, 2402442 (2024).

40. Wouda, P. T., Schmid, M., Nieuwenhuys, B. E. & Varga, P. STM study of the (111) and (100) surfaces of PdAg. *Surf. Sci.* **417**, 292–300 (1998).

41. Gauthier, Y. Pt-Metal Alloy Surfaces: Systematic Trends. *Surface Review and Letters* **3**, 1663–1689 (1996).

42. Ritz, G., Schmid, M., Biedermann, A. & Varga, P. Strain-induced local surface chemical ordering observed by STM. *Phys. Rev. B* **53**, 16019–16026 (1996).

43. Jung, T., Mo, Y. W. & Himpsel, F. J. Identification of Metals in Scanning Tunneling Microscopy via Image States. *Phys. Rev. Lett.* **74**, 1641–1644 (1995).

44. Schmid, M., Stadler, H. & Varga, P. Direct Observation of Surface Chemical Order by Scanning Tunneling Microscopy. *Phys. Rev. Lett.* **70**, 1441–1444 (1993).

45. Choi, Y. J. *et al.* Surface alloy formation of Fe on Cr(100) studied by scanning tunneling microscopy. *Phys. Rev. B* **59**, 10918–10922 (1999).

46. Mo, Y. W. & Himpsel, F. J. Spectroscopic signature of Cu on W(110) from scanning tunneling microscopy and inverse photoemission. *Phys. Rev. B* **50**, 7868–7871 (1994).

47. Nascimento, V. B. *et al.* Surface geometric and electronic structures of BaFe2As2(001). *Phys. Rev. Lett.* **103**, 076104 (2009).

48. Heinz, K., Saldin, D. K. & Pendry, J. B. Diffuse LEED and Surface Crystallography. *Phys. Rev. Lett.* **55**, 2312–2315 (1985).

49. Saldin, D. K., Pendry, J. B., Hove, M. A. Van & Somorjai, G. A. Interpretation of diffuse low-energy electron diffraction intensities. *Phys. Rev. B* **31**, 1216–1218 (1985).

50. Lee, C. *et al.* Lattice-Distortion-Enhanced Yield Strength in a Refractory High-Entropy Alloy. *Advanced Materials* **32**, 2004029 (2020).

51. Lee, C. *et al.* Lattice distortion in a strong and ductile refractory high-entropy alloy. *Acta Mater.* **160**, 158–172 (2018).

52. Fenter, P. & Gustafsson, T. Structural analysis of the Pt(110)-(1×2) surface using medium-energy ion scattering. *Phys. Rev. B* **38**, 10197–10204 (1988).

53. Hannon, J. B., Plummer, E. W., Wentzcovitch, R. M. & Lam, P. K. The (1x3) missing-row surface structure of Be(112-bar0). *Surf. Sci.* **269/270**, 7–13 (1992).

54. Schneeweiss, O. *et al.* Magnetic properties of the CrMnFeCoNi high-entropy alloy. *Phys. Rev. B* **96**, 014437 (2017).

55. Mizuno, M., Sugita, K. & Araki, H. Prediction of short-range order in CrMnFeCoNi high-entropy alloy. *Results Phys.* **34**, 105285 (2022).

56. Laurent-Brocq, M. *et al.* Insights into the phase diagram of the CrMnFeCoNi high entropy alloy. *Acta Mater.* **88**, 355–365 (2015).

57. Hafner, J. Ab-initio simulations of materials using VASP: Density-functional theory and beyond. *J. Comput. Chem.* **29**, 2044–2078 (2008).

58. Kresse, G. & Joubert, D. From ultrasoft pseudopotentials to the projector augmented-wave method. *Phys. Rev. B* **59**, 1758 (1999).

59. Van de Walle, A., Asta, M. & Ceder, G. The alloy theoretic automated toolkit: A user guide. *Calphad* **26**, 539–553 (2002).

60. Perdew, J. P., Burke, K. & Ernzerhof, M. Generalized Gradient Approximation Made Simple. *Phys. Rev. Lett.* **77**, 3865 (1996).

61. Monkhorst, H. J. & Pack, J. D. Special points for Brillouin-zone integrations. *Phys. Rev. B* **13**, 5188 (1976).

62. Tersoff, J. & Hamann, D. R. Theory of the scanning tunneling microscope. *Phys. Rev. B* **31**, 805–813 (1985).

63. Tersoff, J. Method for the calculation of scanning tunneling microscope images and spectra. *Phys. Rev. B* **40**, 11990–11993 (1989).

64. Chien, T. STM, LEED and DFT atomic coordinate data of HEA Cantor alloy. doi:10.6084/m9.figshare.31286263.

**Acknowledgements:** The sample fabrication, characterization, STM measurements and analysis, and DFT calculations are supported by National Science Foundation DMR-2219416 (TYC, GB), and CMMI-2436601 (GB). Insightful discussion on the short-range order is supported by DMR-1611180 (PKL), DMR-1809640 (PKL), and DMR-2226508 (PKL). C.-W.T. and J.-W.Y. thank financial support from the High Entropy Materials Center as part of the Featured Areas Research Center Program, within the framework of the Higher Education Sprout Project by the Ministry of Education (MOE) and also from Project National Science and Technology Council (NSTC) 113-2221-E-007-036 (CWT, JWY) and 112-2221-E-007-032 (CWT, JWY) of the National Science and Technology Council (NSTC) in Taiwan. EWH thanks the support of the NSTC under Grants NSTC 113-2811-E-A49-525 (EWH), 113-2221-E-A49-003 (EWH), and 114-2923-E-A49-003-MY3 (EWH).

**Author Contributions:** T.Y.C. conceived and designed the experiments, analysis, and interpretation of the data. L.K. performed measurements and analyzed experimental data. P.S. and G.B. prepared the HEA sample. P.S. performed DFT calculations. C.-W.T., E.-W.H., P.K.L., and J.-W.Y. contributed intellectually to the short-range order discussions. All authors discussed the results and commented on the manuscript.

**Competing Interest:** The authors declare no competing interests.

**Editor's Summary**

The surface chemical ordering in high entropy alloys is revealed by the surface sensitive imaging tool - scanning tunneling microscopy – which is enabled by the subtle differences in the partial density of states among different elements.

**Peer review information:** *Nature Communications* thanks Shuai Guo, Cheng Yang, and the other, anonymous, reviewer(s) for their contribution to the peer review of this work. A peer review file is available.